NANO LETTERS
Cite This: Nano Lett. XXXX, XXX, XXX−XXX
Letter
pubs.acs.org/NanoLett

Electrically Tunable Exciton−Plasmon Coupling in a WSe_2 Monolayer Embedded in a Plasmonic Crystal Cavity

Alan M. Dibos,[†] You Zhou,[†,‡] Luis A. Jauregui,[‡] Giovanni Scuri,[‡] Dominik S. Wild,[‡] Alexander A. High,[†,‡] Takashi Taniguchi,[§] Kenji Watanabe,[§] Mikhail D. Lukin,[‡] Philip Kim,[‡] and Hongkun Park*[,†,‡]

[†]Department of Chemistry and Chemical Biology and [‡]Department of Physics, Harvard University, Cambridge, Massachusetts 02138, United States

[§]National Institute for Materials Science, 1-1 Namiki, Tsukuba 305-0044, Japan

Supporting Information

ABSTRACT: We realize a new electroplasmonic switch based upon electrically tunable exciton−plasmon interactions. The device consists of a hexagonal boron nitride (hBN)-encapsulated tungsten diselenide (WSe_2) monolayer on top of a single-crystalline silver substrate. The ultrasmooth silver substrate serves a dual role as the medium to support surface plasmon polaritons (SPPs) and the bottom gate electrode to tune the WSe_2 exciton energy and brightness through electrostatic doping. To enhance the exciton−plasmon coupling, we implement a plasmonic crystal cavity on top of the hBN/WSe_2/hBN/Ag heterostructure with a quality factor reaching 550. The tight confinement of the SPPs in the plasmonic cavity enables strong coupling between excitons and SPPs when the WSe_2 exciton absorption is resonant with the cavity mode, leading to a vacuum Rabi splitting of up to 18 meV. This strong coupling can also be switched off with the application of a modest gate voltage that increases the doping density in the monolayer. This demonstration paves the way for new plasmonic modulators and a general device architecture to enhance light-matter interactions between SPPs and various embedded emitters.

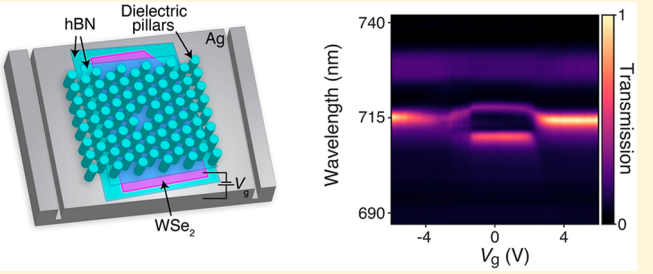

KEYWORDS: *Transition metal dichalcogenides, surface plasmon polaritons, electrically tunable interaction, vacuum Rabi splitting*

Engineering hybridized states of excitons and photons, known as exciton−polaritons,[1,2] opens up exciting new fundamental physics research[3] and forms the basis for interesting device applications, such as ultrafast optoelectronics[4] and all-optical logic.[5] Transition metal dichalcogenide (TMD) monolayers exhibit many properties that are suitable for next-generation exciton−polariton devices. They host strongly bound excitons that may enable room temperature polaritonics.[1] The absorption wavelengths of TMD excitons depend on the material composition of the monolayer and span the visible to telecommunications regimes.[6−12] In addition, the lack of dangling bonds on these materials enables the creation of high-quality interfaces via simple stacking, thus enabling formation of various heterostructures[13] that can easily be transferred onto other functional substrates.[14]

Exploiting these favorable physical properties, there have been several excellent demonstrations of strong exciton−photon coupling, using various types of optical resonators, including dielectric mirror cavities,[11,15,16] metallic mirror cavities,[17,18] plasmonic hole arrays,[17,19] and localized surface plasmon particles/arrays.[19,20] In several of these experiments, the authors were able to demonstrate fine control of the exciton−photon or exciton−plasmon coupling strength by electrically gating the monolayer.[11,18,20] Furthermore, there have been demonstrations of large Rabi splittings with magnitudes in excess of 100 meV, even at room temperature.[17,19]

In this Letter, we explore an alternative device strategy to realize electrically tunable strong coupling between TMD excitons and surface plasmon polaritons (SPPs) by placing a WSe_2 monolayer encapsulated by hexagonal boron nitride (hBN) flakes on top of a single-crystalline silver (Ag) film. Because of their evanescent nature, SPPs enable confinement of light near the metal surface well below the diffraction limit, making them uniquely suited for coupling to excitons in TMD monolayers.[21] We further enhance the exciton−plasmon interaction by embedding the hBN/WSe_2/hBN van der Waals heterostructure in a novel plasmonic crystal cavity with a quality factor above 500, thus enabling strong coupling between TMD excitons and the cavity SPPs. By electrically tuning the Fermi level of the TMD monolayer, we show that such a device can function as an electroplasmonic modulator

Received: February 1, 2019
Revised: May 12, 2019

DOI: 10.1021/acs.nanolett.9b00484
Nano Lett. XXXX, XXX, XXX−XXX

that utilizes the strong coupling between excitons and plasmons. Importantly, the presented device platform for switchable coupling between SPP modes and embedded emitters can be fully integrated in on-chip systems.

Critical to our device architecture are the multiple functionalities of two key components, the silver substrate and the hexagonal boron nitride (hBN) layers. The ultrasmooth single-crystalline silver film[22] serves as the medium that supports low-loss SPPs as well as a bottom gate electrode (see Methods); the SPP propagation lengths on this silver film reaches hundreds of micrometers near the exciton resonance of WSe_2 at ∼715 nm.[22] Similarly, the hBN layers also serve several important functions within the device. The bottom hBN flake is a gate dielectric and a physical spacer between the WSe_2 and Ag film. Because the thickness of this bottom flake is only 8−10 nm, the WSe_2 monolayer is kept close to the electric field maximum of the SPP mode while not touching the metal surface directly. The top hBN flake encapsulates the WSe_2 monolayer, improving its optical response.[23] It is important to note that the plasmons propagating along the silver/bottom hBN interface have an evanescent tail that extends beyond the top hBN layer (+z direction in Figure 1c). Thus, dielectric structures on top of the heterostructure, such as a waveguide or a periodic array of pillars, can still be used to engineer the propagation of the SPPs.

Before we construct a plasmonic crystal cavity device with an embedded WSe_2 monolayer, we first characterize the exciton absorption resonances in monolayer WSe_2 via SPP transmission experiments. Specifically, we use a combination of electron beam lithography, atomic layer deposition of TiO_2, and reactive ion etching to define a TiO_2 dielectric waveguide (width, 200 nm; length, 5 μm; refractive index n = 2.38) on top of the hBN/WSe_2/hBN heterostructure and Ag substrate (Figure 1a). We then measure the SPP transmission through the waveguide as a function of the gate voltage (V_g) applied to the silver. Our measurements are performed in a cryostat (T = 4 K) equipped with a two-channel confocal microscope where we are able to excite and collect from spatially distinct diffraction-limited spots. Because of the wavevector mismatch between free space photons and SPPs, we use a broadband scattering center to convert white laser light focused at the one end of the TiO_2 waveguide into SPPs that propagate along the Ag/WSe_2/TiO_2 interface (see Supporting Information). We then collect light scattered at the opposite end of the waveguide (Figure 1b, inset) and analyze it via a spectrometer equipped with a charge coupled device (CCD) (see Methods).

As we sweep the gate voltage applied to the silver, we observe spectral regions of decreased transmission, signifying the absorption of SPPs via the creation of WSe_2 excitons (Figure 1b). The absorption is dominated by neutral excitons (X_0) near zero gate voltage;[24] at larger gate voltages ($|V_g| > 2$ V), however, the magnitude of neutral exciton absorption decreases dramatically and broader red-shifted absorption features emerge. The appearance of the broader absorption features at $V_g > 2$ V ($V_g < -2$ V) correlates with increased conductivity of the WSe_2 monolayer, indicating that these absorption features are associated with electron (hole) doping (see Supporting Information). Previous studies have shown that these features are associated with absorption from charged excitons[7,16,18,25] (X^- or X^+) or Fermi polarons.[11]

Once we verify efficient coupling of excitons and SPPs, we embed a hBN/WSe_2/hBN heterostructure into a plasmonic crystal cavity (Figure 1c), in which an array of dielectric posts

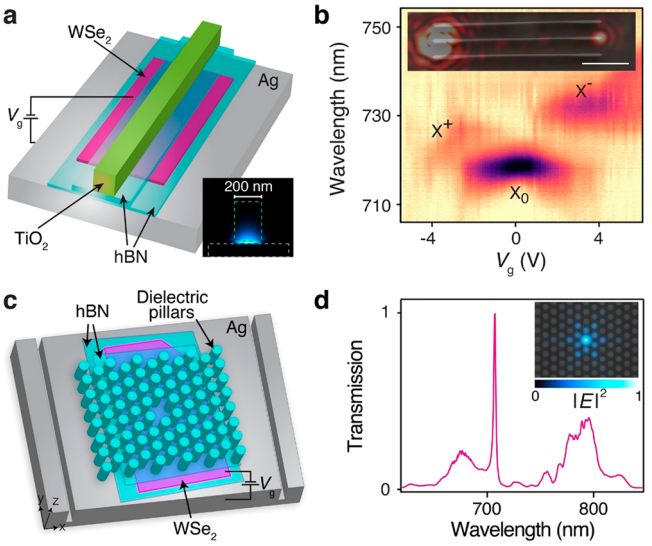

Figure 1. Monolayer WSe_2 incorporated into two different plasmonic device architectures using a single crystalline Ag substrate. (a) Schematic of the plasmonic waveguide with a WSe_2 monolayer as the electrically tunable absorber. Inset: Cross-section of the simulated electric field mode supported by the TiO_2 waveguide (green) on Ag (gray). (b) TiO_2 waveguide-assisted SPP transmission spectra through a WSe_2 monolayer collected as a function of gate voltage. The spectra are collected at T = 4 K, and the absorption feature denoted by X_0 (X^+ and X^-) indicates the neutral (charged) exciton species when the Fermi level is inside (outside) the bandgap region. Inset: Optical image overlaid on a scanning electron microscope image, demonstrating in-coupling (left) and out-coupling (right) at the ends of the TiO_2 tapered waveguide. The scale bar is 3 μm. (c) A schematic of the plasmonic crystal cavity between two trenches etched in the silver that serve as in-coupling and out-coupling structures for surface plasmon polaritons (SPPs). The cavity is defined by dielectric pillars atop the WSe_2 monolayer with a single pillar missing to form the cavity defect. (d) Transmission through a bare plasmonic crystal cavity (without WSe_2) shows a stopband ranging from 680 to 780 nm with a pronounced cavity peak centered near 709 nm. The fabricated cavities have quality factors of up to 550. Inset: The simulated electric field intensity of the cavity mode, overlaid on a scanning electron microscope image of the fabricated device.

on top of the heterostructure and Ag substrate creates a plasmonic stop-band. The incorporation of a cavity defect, a single missing dielectric pillar in a hexagonal array (lattice constant, 346 nm; pillar diameter, 200 nm; pillar height, ∼200 nm) within the stop band, completes the plasmonic analog of a single-defect photonic crystal cavity.[26−28] We use lithographically defined ZEP electron beam resist as the dielectric pillar material (see Methods) because it has a refractive index of n = 1.57 and can be patterned with nanometer resolution. A finite difference time domain simulation of our plasmonic crystal cavity (Figure 1d inset) shows that the electromagnetic fields are spatially confined to the region near the missing pillar, thus yielding a cavity with a mode volume of $0.1\lambda^3$ and a narrow resonance within the plasmonic bandgap.

We experimentally characterize the cavity by shining white light laser into a silver trench to launch SPPs into the cavity. We determine the cavity transmission spectrum by collecting SPPs that scatter into free space photons at the far Ag trench. The experimental transmission spectrum of a typical plasmonic crystal cavity without an embedded hBN/WSe_2/hBN heterostructure shows a stopband ranging from 680 to 780 nm with a pronounced cavity resonance at 709 nm. The quality factor of

DOI: 10.1021/acs.nanolett.9b00484
Nano Lett. XXXX, XXX, XXX−XXX

our plasmonic crystal cavity can be as high as 550 (Figure 1d), a value that is significantly higher than previous plasmonic cavity demonstrations with small mode volumes.[21,29,30]

Optical characterization of a plasmonic crystal cavity with an embedded WSe_2 monolayer reveals evidence for strong coupling between excitons and SPPs (Figures 2 and 3). In this device, we launch SPPs into the cavity at the left trench and collect photons from plasmons that scatter into free space near the cavity defect (Figure 2a, see Methods). We then analyze the spectrum of these scattered SPPs as we tune the cavity resonance wavelength via gas tuning (see Methods) while fixing the gate voltage applied to the silver at zero. As we sweep the cavity wavelength through the WSe_2 neutral exciton (X_0) absorption (λ = 713 nm), we observe a clear anticrossing of the cavity mode and the neutral exciton (Figure 2b). This avoided crossing of 18 meV arises due to vacuum Rabi splitting[20,31] from the hybridization of the excitons in WSe_2 with the plasmonic crystal cavity mode (Figure 2c). By fitting the transmission spectra, we extract the value of the energy splitting to be 18.2 meV (see Supporting Information). This value is larger than the sum of the widths of the cavity (7 meV) and exciton (7.5 meV) modes (extracted from measurements of bare cavity transmission and exciton absorption), satisfying the criteria for strong coupling. We also tuned the same cavity through the negatively charged exciton absorption resonance (X^-). Although the coupling between SPPs and charged excitons leads to modified SPP transmission, we did not observe a complete mode splitting (see Supporting Information).

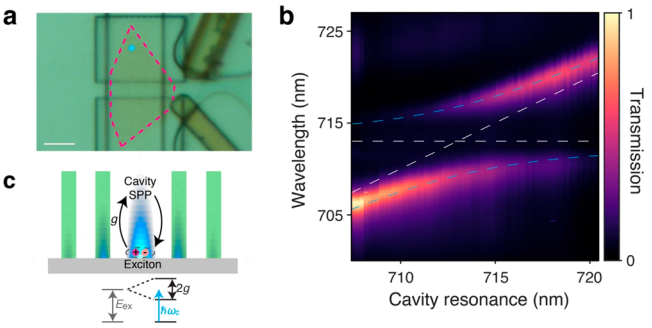

Figure 2. Rabi splitting in an integrated monolayer WSe_2 plasmonic crystal cavity. (a) Optical image of a plasmonic crystal cavity device showing the WSe_2 flake (outlined with dashed magenta) and the missing pillar (light blue dot) as the cavity defect. The WSe_2 monolayer is electrically contacted with a Au electrode. The SPPs are launched by focusing a diffraction-limited laser spot on the long left vertical trench etched into the silver film. The scale bar is 3 μm. (b) SPP transmission spectra of the plasmonic crystal cavity display an avoided crossing as the cavity is tuned in situ through the exciton absorption resonance. The white dashed lines show the uncoupled exciton and plasmonic crystal cavity mode, whereas the dashed blue curves correspond to theoretical fits of the hybrid states using a coupled oscillator model. (c) A schematic of vacuum Rabi splitting due to the strong coupling of a two-level system (exciton) with the plasmonic crystal cavity mode.

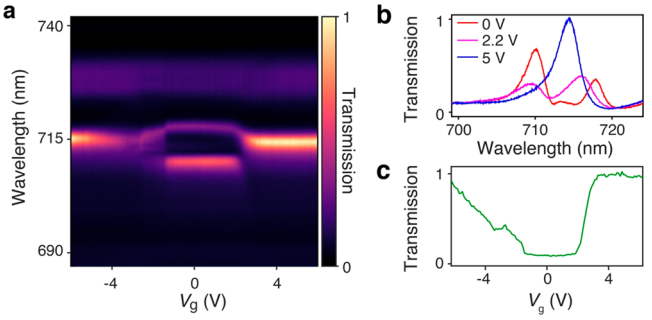

Figure 3. Electrically tunable transmission through a monolayer WSe_2 plasmonic crystal cavity. (a) Cavity transmission as a function of gate voltage. (b) Transmission spectra for three different gate voltages when the plasmonic crystal cavity is resonant with the exciton absorption in WSe_2. At gate voltages of 0 and 2.2 V, the transmission splits into two peaks as the WSe_2 neutral exciton absorption is tuned onto resonance with the cavity, with a maximum separation of 18 meV as in Figure 2b. As the doping concentration in the monolayer is increased at larger bias voltages, the neutral exciton absorption is suppressed leading to a single peak near 715 nm in the stopband (such as at V_g > 3 V). (c) Line cut of the cavity transmission at 715 nm, showing up to 90% absorption.

In our plasmonic crystal cavity, we can turn on/off the strong coupling between WSe_2 excitons SPPs by doping the monolayer using the silver bottom gate and thus by changing the exciton absorption strength and energy. When we fix the cavity resonance to the neutral exciton wavelength and launch SPPs into the cavity, the light scattered near the cavity defect shows a split resonance at zero gate voltage. As we sweep the gate voltage toward V_g = 5 V (−5 V) and dope the monolayer with electrons (holes), however, the split resonance disappears (Figure 3a). The split resonance at zero gate voltage is due to the same vacuum Rabi splitting as in Figure 2b. This split resonance at V_g = 0 V is clearly wider than the single cavity mode at V_g = 5 V (Figure 3b). The broad feature near 725 nm is due to transmitted SPPs arising from imperfections in the cavity fabrication and does not couple strongly to excitons or charged excitons. The light scattered near the cavity defect can be reduced by more than 90% at the neutral exciton wavelength (λ = 715 nm) as the gate voltage is swept from +3.5 to 0 V (Figure 3c). These results indicate that our TMD−plasmonic crystal cavity platform can serve as an electro-plasmonic modulator that allows switching from an absorptive to a transmissive state by the application of a <5 V gate voltage pulse instead of the much larger voltages needed in other TMD strong coupling demonstrations that employ thick SiO_2 gate dielectrics.[11,20]

A simple theoretical model that accounts for the strong excitonic transition and the tight confinement of the plasmonic cavity mode provides an excellent account of the Rabi splitting observed in our cavity device (see Supporting Information). The cavity mode is characterized by its confinement length $l \approx$ 6.5 μm, normal to the plane of the WSe_2 monolayer, which we computed using a numerical simulation of the mode profile. The exciton transition strength can be parametrized in terms of the dimensionless quantity $\beta = |\varphi(0)|^2 |r_{cv}|^2$, where $\varphi(0)$ is the exciton wave function at zero separation between the hole and the electron, and r_{cv} denotes the transition dipole matrix element between the valence and conduction band. The parameters β and l are then related to the coupling rate g, the rate at which energy transfers between excitons in the TMD and cavity SPPs, by $g^2 = \frac{e^2\beta}{\epsilon_0 l}\hbar\omega_c$ where e is the electron charge, ω_c is the cavity frequency, $\hbar$ is the reduced Planck's constant, and ϵ_0 is the free space permittivity. The normal mode splitting between the two exciton-polaritons is given by $\sqrt{4g^2 + \delta^2}$,

DOI: 10.1021/acs.nanolett.9b00484
Nano Lett. XXXX, XXX, XXX−XXX

where δ denotes the detuning between the exciton resonance and the cavity mode.

By fitting an analytic expression for the cavity transmission spectrum to the measured spectrum (Figure 3b, blue dashed lines), we extract $\beta \approx 1.7 \times 10^{-2}$, which is consistent with results from previous ab initio calculations.[9,32−34] The measured value of β further enables the computation of the spontaneous emission rate of an exciton in free space. We obtain a radiative line width of $\gamma_f \approx 2.6$ meV, which is in good agreement with values reported elsewhere.[35−38]

Further improvements are possible to allow for a larger Rabi splitting and enhanced device functionality. The primary limitation of our device geometry is the fact that the dominant electric field component in the plasmonic crystal cavity mode is oriented normal to the plane of the Ag film (in the +z-direction as indicated in Figure 1a), whereas the excitons in WSe_2 have a dipole orientation primarily in the plane of the monolayer.[39] However, such a cavity design would be useful for enhancing the emission rate of many other emitters in 2D materials with out-of-plane electric dipole moments, including dark excitons in monolayer WSe_2[39] as well as interlayer excitons in multilayer TMDs.[40] Furthermore, our plasmonic crystal cavity design is agnostic about the material of interest as long as it is sufficiently thin to enable evanescent electric field penetration through the layer and into the dielectric pillars above. Therefore, coupling to other quantum emitters such as terrylene molecules doped into crystalline p-terphenyl films[41] or defect centers in diamond and 4H-SiC can be achieved using photoelectrochemically etched membranes.[42,43] These systems have the potential to realize a larger collective Rabi splitting or efficient coupling to an individual emitter, thereby enabling plasmon switches with high contrast at higher temperatures.

METHODS

Sample Structure and Fabrication. Single-crystalline silver films were grown on the Si face of undoped 4H-SiC (0001) wafers by magnetron sputtering at 350 °C with a 90 nm thick epitaxial Ti layer as the buffer layer sputtered at 500 °C (detailed methods will be reported elsewhere). All the heterostructures on Ag were made using a dry-transfer process from exfoliated monolayers,[44] which preserved the ultrasmooth surface of the single-crystalline silver.

The hBN thicknesses were characterized using atomic force microscopy, allowing us to control the spacer layer between the Ag substrate and WSe_2. The device onto which we placed the waveguide in Figure 1b had a 10 nm bottom hBN layer, and the plasmonic cavity device in Figures 2 and 3 had a bottom hBN spacer of 8 nm.

Two different approaches were employed to make source and drain contacts to the WSe_2 monolayer, top Cr/Au (10 nm/80 nm) contacts and bottom Pt contacts (8 nm), both fabricated by electron beam lithography and lift-off processes. For top Cr/Au contacts, the thermally evaporated metal contacted the region of the WSe_2 that was not covered by the top hBN. On the other hand, bottom Pt contacts were deposited by electron-beam evaporation on the bottom hBN before the WSe_2 monolayer, completely covered by an hBN passivation layer, was transferred onto the bottom hBN. Bottom Pt contacts typically exhibited lower contact resistance as compared with top Cr/Au contact. In both cases, we used a bilayer of 160 nm thick Si_3N_4 and 30 nm thick alumina, grown by plasma-enhanced chemical vapor deposition and atomic layer deposition (ALD), respectively, as insulating barriers to prevent an electrical short circuit between the Ag substrate and the source-drain leads.

In the cavity experiments, we first etched trenches into the single crystal Ag film by e-beam lithography and Ar ion milling, and then the hBN/WSe_2/hBN heterostructures were stamped between the trenches. The cavity was realized by patterning ZEP-520A (diluted 1:1 with anisole) via e-beam lithography to expose the unwanted areas leaving behind pillars of ZEP on the top-hBN surface.

Optical Characterization. Optical measurements were performed in a home-built confocal microscope equipped with a cryostat. For the absorption/transmission measurements, either a NKT SuperK supercontinuum laser or a broadband LED was focused by a 100× objective (NA 0.75) as the excitation source. Mirrors mounted on two galvanometers were used to scan the incoming beam and the collection spot independently. The light from the collection spot is analyzed with a spectrometer (f = 300 mm) using either a 50 or 1200 grooves/mm grating. The resultant spectrum is imaged using a thermoelectrically cooled CCD.

For the TiO_2 waveguide-assisted SPP absorption measurements (Figure 1b), the excitation and collection spots were focused on the opposite ends of the waveguide. For the bare plasmonic crystal cavity measurements shown in Figure 1d, the excitation spot was focused on the left trench in the Ag to launch SPPs in the + x-direction (as indicated in Figure 1a). The collection spot was positioned on the right trench and in line with the cavity defect. Finally, for the WSe_2-coupled plasmonic cavity device measured in Figures 2 and 3 and shown in Figure 2a, the excitation spot was focused at the left trench and the collection spot was aligned to the cavity defect. This measurement configuration was necessary due to misalignment between the far trench and the dielectric pillars during the electron-beam lithography step, which lead to a greatly reduced transmission signal. Previous measurements on bare devices suggested similar spectra for scattered SPPs from the far trench and cavity defect. During the plasmonic crystal cavity measurements, the resonance wavelength was red shifted in situ by condensing N_2 gas on the surface of the ZEP pillars at low temperature.

ASSOCIATED CONTENT

Supporting Information

The Supporting Information is available free of charge on the ACS Publications website at DOI: 10.1021/acs.nanolett.9b00484.

Details about hBN encapsulation, additional TiO_2 waveguide-assisted SPP absorption spectra, a higher-resolution plasmonic crystal cavity transmission spectrum, and the vacuum Rabi splitting theory (PDF)

AUTHOR INFORMATION

Corresponding Author

*E-mail: hongkun_park@harvard.edu.

ORCID

Giovanni Scuri: 0000-0003-1050-3114

Philip Kim: 0000-0002-8255-0086

Hongkun Park: 0000-0001-9576-8829

Notes

The authors declare no competing financial interest.

DOI: 10.1021/acs.nanolett.9b00484
Nano Lett. XXXX, XXX, XXX−XXX

■ ACKNOWLEDGMENTS

We acknowledge support from the DoD Vannevar Bush Faculty Fellowship (N00014-16-1-2825 for HP, N00014-18-1-2877 for PK), NSF (PHY-1506284 for HP and MDL), NSF CUA (PHY-1125846 for HP and MDL), AFOSR MURI (FA9550-17-1-0002), ARL (W911NF1520067 for HP and MDL), the Gordon and Betty Moore Foundation (GBMF4543 for PK), ONR MURI (N00014-15-1-2761 for PK), and Samsung Electronics (for PK and HP). The device fabrication was carried out at the Harvard Center for Nanoscale Systems.

■ REFERENCES

(1) Sanvitto, D.; Kena-Cohen, S. *Nat. Mater.* **2016**, *15*, 1061−1073.
(2) Weisbuch, C.; Nishioka, M.; Ishikawa, A.; Arakawa, Y. *Phys. Rev. Lett.* **1992**, *69*, 3314−3317.
(3) Byrnes, T.; Kim, N. Y.; Yamamoto, Y. *Nat. Phys.* **2014**, *10*, 803−813.
(4) Dreismann, A.; Ohadi, H.; del Valle-Inclan Redondo, Y.; Balili, R.; Rubo, Y. G.; Tsintzos, S. I.; Deligeorgis, G.; Hatzopoulos, Z.; Savvidis, P. G.; Baumberg, J. J. *Nat. Mater.* **2016**, *15*, 1074−1078.
(5) Ballarini, D.; De Giorgi, M.; Cancellieri, E.; Houdré, R.; Giacobino, E.; Cingolani, R.; Bramati, A.; Gigli, G.; Sanvitto, D. *Nat. Commun.* **2013**, *4*, 1778.
(6) Jones, A. M.; Yu, H.; Ghimire, N. J.; Wu, S.; Aivazian, G.; Ross, J. S.; Zhao, B.; Yan, J.; Mandrus, D. G.; Xiao, D.; Yao, W.; Xu, X. *Nat. Nanotechnol.* **2013**, *8*, 634−638.
(7) Mak, K. F.; He, K.; Lee, C.; Lee, G. H.; Hone, J.; Heinz, T. F.; Shan, J. *Nat. Mater.* **2013**, *12*, 207−211.
(8) Ross, J. S.; Wu, S.; Yu, H.; Ghimire, N. J.; Jones, A. M.; Aivazian, G.; Yan, J.; Mandrus, D. G.; Xiao, D.; Yao, W.; Xu, X. *Nat. Commun.* **2013**, *4*, 1474.
(9) Chernikov, A.; van der Zande, A. M.; Hill, H. M.; Rigosi, A. F.; Velauthapillai, A.; Hone, J.; Heinz, T. F. *Phys. Rev. Lett.* **2015**, *115*, 126802.
(10) Scharf, B.; Wang, Z.; Van Tuan, D.; Shan, J.; Mak, K. F.; Zutic, I.; Dery, H. *Phys. Rev. B* **2019**, *99*, 085301.
(11) Sidler, M.; Back, P.; Cotlet, O.; Srivastava, A.; Fink, T.; Kroner, M.; Demler, E.; Imamoglu, A. *Nat. Phys.* **2017**, *13*, 255−261.
(12) Sun, Z.; Martinez, A.; Wang, F. *Nat. Photonics* **2016**, *10*, 227−238.
(13) Geim, A. K.; Grigorieva, I. V. *Nature* **2013**, *499*, 419−425.
(14) Wu, S.; Buckley, S.; Schaibley, J. R.; Feng, L.; Yan, J.; Mandrus, D. G.; Hatami, F.; Yao, W.; Vučković, J.; Majumdar, A.; et al. *Nature* **2015**, *520*, 69−72.
(15) Liu, X.; Galfsky, T.; Sun, Z.; Xia, F.; Lin, E.-c.; Lee, Y.-H.; Kéna-Cohen, S.; Menon, V. M. *Nat. Photonics* **2015**, *9*, 30−34.
(16) Dufferwiel, S.; Schwarz, S.; Withers, F.; Trichet, A. A. P.; Li, F.; Sich, M.; Del Pozo-Zamudio, O.; Clark, C.; Nalitov, A.; Solnyshkov, D. D.; Malpuech, G.; Novoselov, K. S.; Smith, J. M.; Skolnick, M. S.; Krizhanovskii, D. N.; Tartakovskii, A. I. *Nat. Commun.* **2015**, *6*, 8579.
(17) Wang, S.; Li, S.; Chervy, T.; Shalabney, A.; Azzini, S.; Orgiu, E.; Hutchison, J. A.; Genet, C.; Samorì, P.; Ebbesen, T. W. *Nano Lett.* **2016**, *16*, 4368−4374.
(18) Chakraborty, B.; Gu, J.; Sun, Z.; Khatoniar, M.; Bushati, R.; Boehmke, A. L.; Koots, R.; Menon, V. M. *Nano Lett.* **2018**, *18*, 6455−6460.
(19) Cuadra, J.; Baranov, D. G.; Wersäll, M.; Verre, R.; Antosiewicz, T. J.; Shegai, T. *Nano Lett.* **2018**, *18*, 1777−1785.
(20) Lee, B.; Liu, W.; Naylor, C. H.; Park, J.; Malek, S. C.; Berger, J. S.; Johnson, A. T. C.; Agarwal, R. *Nano Lett.* **2017**, *17*, 4541−4547.
(21) de Leon, N. P.; Shields, B. J.; Yu, C. L.; Englund, D. E.; Akimov, A. V.; Lukin, M. D.; Park, H. *Phys. Rev. Lett.* **2012**, *108*, 226803.
(22) High, A. A.; Devlin, R. C.; Dibos, A.; Polking, M.; Wild, D. S.; Perczel, J.; de Leon, N. P.; Lukin, M. D.; Park, H. *Nature* **2015**, *522*, 192−196.
(23) Scuri, G.; Zhou, Y.; High, A. A.; Wild, D. S.; Shu, C.; De Greve, K.; Jauregui, L. A.; Taniguchi, T.; Watanabe, K.; Kim, P.; Lukin, M. D.; Park, H. *Phys. Rev. Lett.* **2018**, *120*, 037402.
(24) You, Y.; Zhang, X.-X.; Berkelbach, T. C.; Hybertsen, M. S.; Reichman, D. R.; Heinz, T. F. *Nat. Phys.* **2015**, *11*, 477−481.
(25) Ross, J. S.; Wu, S.; Yu, H.; Ghimire, N. J.; Jones, A. M.; Aivazian, G.; Yan, J.; Mandrus, D. G.; Xiao, D.; Yao, W.; et al. *Nat. Commun.* **2013**, *4*, 1474.
(26) Akahane, Y.; Asano, T.; Song, B.-S.; Noda, S. *Nature* **2003**, *425*, 944−947.
(27) Levy, J. S.; Gondarenko, A.; Foster, M. A.; Turner-Foster, A. C.; Gaeta, A. L.; Lipson, M. *Nat. Photonics* **2010**, *4*, 37−40.
(28) Gan, X.; Shiue, R.-J.; Gao, Y.; Mak, K. F.; Yao, X.; Li, L.; Szep, A.; Walker, D., Jr; Hone, J.; Heinz, T. F.; et al. *Nano Lett.* **2013**, *13*, 691−696.
(29) Hoang, T. B.; Akselrod, G. M.; Mikkelsen, M. H. *Nano Lett.* **2016**, *16*, 270−5.
(30) Chorsi, H. T.; Youngkyu, L.; Alu, A.; Zhang, J. X. J. *Sci. Rep.* **2017**, *7*, 15985.
(31) Bellessa, J.; Symonds, C.; Meynaud, C.; Plenet, J. C.; Cambril, E.; Miard, A.; Ferlazzo, L.; Lemaître, A. *Phys. Rev. B: Condens. Matter Mater. Phys.* **2008**, *78*, 205310.
(32) Xiao, D.; Liu, G.-B.; Feng, W.; Xu, X.; Yao, W. *Phys. Rev. Lett.* **2012**, *108*, 196802.
(33) Berkelbach, T. C.; Hybertsen, M. S.; Reichman, D. R. *Phys. Rev. B: Condens. Matter Mater. Phys.* **2013**, *88*, 045318.
(34) Fang, S.; Defo, R. K.; Shirodkar, S. N.; Lieu, S.; Tritsaris, G. A.; Kaxiras, E. *Phys. Rev. B: Condens. Matter Mater. Phys.* **2015**, *92*, 205108.
(35) Moody, G.; Dass, C. K.; Hao, K.; Chen, C.-H.; Li, L.-J.; Singh, A.; Tran, K.; Clark, G.; Xu, X.; Berghäuser, G. *Nat. Commun.* **2015**, *6*, 8315.
(36) Palummo, M.; Bernardi, M.; Grossman, J. C. *Nano Lett.* **2015**, *15*, 2794−2800.
(37) Pöllmann, C.; Steinleitner, P.; Leierseder, U.; Nagler, P.; Plechinger, G.; Porer, M.; Bratschitsch, R.; Schüller, C.; Korn, T.; Huber, R. *Nat. Mater.* **2015**, *14*, 889−893.
(38) Zhou, Y.; Scuri, G.; Sung, J.; Gelly, R. J.; Wild, D. S.; De Greve, K.; Joe, A. Y.; Taniguchi, T.; Watanabe, K.; Kim, P.; Lukin, M. D.; Park, H. arXiv:1901.08500 **2019** (accessed May 23, 2019).
(39) Zhou, Y.; Scuri, G.; Wild, D. S.; High, A. A.; Dibos, A.; Jauregui, L. A.; Shu, C.; De Greve, K.; Pistunova, K.; Joe, A.; et al. *Nat. Nanotechnol.* **2017**, *12*, 856−860.
(40) Yu, H.; Liu, G.-B.; Yao, W. *2D Mater.* **2018**, *5*, 035021.
(41) Pfab, R. J.; Zimmermann, J.; Hettich, C.; Gerhardt, I.; Renn, A.; Sandoghdar, V. *Chem. Phys. Lett.* **2004**, *387*, 490−495.
(42) Magyar, A. P.; Lee, J. C.; Limarga, A. M.; Aharonovich, I.; Rol, F.; Clarke, D. R.; Huang, M.; Hu, E. L. *Appl. Phys. Lett.* **2011**, *99*, 081913.
(43) Bracher, D. O.; Hu, E. L. *Nano Lett.* **2015**, *15*, 6202−7.
(44) Zomer, P.; Guimarães, M.; Brant, J.; Tombros, N.; van Wees, B. *Appl. Phys. Lett.* **2014**, *105*, 013101.

DOI: 10.1021/acs.nanolett.9b00484
Nano Lett. XXXX, XXX, XXX−XXX